Journal of Thermal Biology 141 (2026) 104570

Contents lists available at ScienceDirect

Journal of Thermal Biology

journal homepage: www.elsevier.com/locate/jtherbio

An integrated experimental–computational electromagnetic–thermal framework for predicting bioheat response of the human head to wearable wireless devices ☆

Ivan Dominik Horvat [a,*], Klementina Vidjak [c], Jana Wedel [b], Jurij Iljaž [a], Blaž Kamenik [a], Dragan Poljak [c], Jure Ravnik [a]

[a] Faculty of Mechanical Engineering, University of Maribor, Smetanova ulica 17, Maribor, 2000, Slovenia
[b] Lehrstuhl für Technische Mechanik, Friedrich-Alexander-Universität Erlangen–Nürnberg, Egerlandstraße 5, Erlangen, 91058, Germany
[c] Faculty of Electrical Engineering, Mechanical Engineering and Naval Architecture, University of Split, Ruđera Boškovića 32, Split, 21000, Croatia

ARTICLE INFO

Keywords:
Bioheat modeling
Electromagnetic exposure
Specific absorption rate (SAR)
Wearable devices
Wireless earbuds
Thermal response
Electromagnetic–thermal coupling
Infrared thermography
OpenFOAM

ABSTRACT

The increasing use of wearable wireless devices operating in close proximity to the human body has raised the need for reliable assessment of electromagnetic exposure and associated thermal effects in biological tissue. In particular, wireless earbuds produce both electromagnetic energy absorption and device self-heating as potential sources of localized temperature elevation near the head. This study presents an integrated experimental–computational–electromagnetic–thermal framework for predicting the bioheat response of the human head. The approach combines infrared thermography measurements on a tissue-mimicking ear phantom with inverse heat-transfer analysis to estimate effective thermal parameters and device-related heat generation. These parameters are incorporated into a 3D bioheat model of an anatomically realistic head. Electromagnetic field distributions are obtained from full-wave simulations of a representative earbud antenna initially designed for the 2.45 GHz ISM band and evaluated at its tissue-loaded resonance near 2.3 GHz, and the resulting spatially resolved pointwise specific absorption rate (SAR) is applied as a volumetric heat source in the thermal model. The coupled problem is solved using a custom OpenFOAM-based bioheat solver. Results show that SAR distributions are highly localized near the ear, whereas the resulting temperature field is smoother due to thermal diffusion. The predicted temperature increase remains confined to the vicinity of the earbud and is relatively small. Device self-heating is identified as the dominant contributor to temperature elevation, while the EM-induced component is comparatively minor. Variations in blood perfusion and tissue thermal conductivity produced only modest changes in the predicted local temperature. The proposed framework provides a consistent and computationally efficient pathway for coupled electromagnetic–thermal analysis, supported by experimental calibration, and is suitable for thermal assessment and design evaluation of wearable wireless devices.

1. Introduction

Wireless technologies are increasingly embedded in everyday life through compact devices that operate continuously and in close proximity to the human body. With the expansion of modern wireless communication systems and the growing use of wearable electronics, exposure scenarios involving near-body devices have become increasingly relevant (Karipidis et al., 2021; Verma et al., 2023).

At radiofrequencies, the dominant established interaction mechanism with biological tissue is energy absorption leading to heating. When the spatial scale of the incident field is comparable to relevant anatomical dimensions, appreciable electromagnetic energy may be deposited in tissue, thereby acting as a volumetric heat source and potentially producing localized temperature elevation (Diao et al., 2025; Hirata et al., 2025). For exposures in the frequency range from 100 kHz to 6 GHz, specific absorption rate (SAR) is the principal dosimetric quantity used to quantify the rate of electromagnetic energy absorption per unit tissue mass. Above the transition frequency of 6 GHz, absorbed power density is commonly used to characterize superficial energy deposition and associated localized heating effects

☆ **Funding:** This work was supported by the Slovenian Research and Innovation Agency, project J7-60118, and the Croatian Science Foundation, project IPS-2024-02-7779.

* Corresponding author.
E-mail address: ivan.horvat@um.si (I.D. Horvat).

https://doi.org/10.1016/j.jtherbio.2026.104570
Received 2 June 2026; Received in revised form 12 August 2026; Accepted 8 September 2026
Available online 14 September 2026
0306-4565/© 2026 The Authors. Published by Elsevier Ltd. This is an open access article under the CC BY license (http://creativecommons.org/licenses/by/4.0/).

Nomenclature

Symbols

Symbol	Definition	Unit
c_p	Specific heat capacity	$J\,kg^{-1}\,K^{-1}$
$c_{p,b}$	Specific heat capacity of blood	$J\,kg^{-1}\,K^{-1}$
d	Distance measured from the pointwise SAR maximum	mm
$\vec{E}$	Electric-field vector	$V\,m^{-1}$
h	Effective surface heat-transfer coefficient	$W\,m^{-2}\,K^{-1}$
J	Least-squares objective function	K^2
k	Thermal conductivity	$W\,m^{-1}\,K^{-1}$
m	Mass	kg
m_i	Mass of computational cell i	kg
N	Number of data points in the objective function	–
$\vec{n}$	Outward unit-normal vector	–
P	Power or heat-release rate	W
$\vec{q}$	Heat-flux vector	$W\,m^{-2}$
q_{ext}	Device-related volumetric heat-generation rate	$W\,m^{-3}$
q_m	Metabolic volumetric heat-generation rate	$W\,m^{-3}$
$\vec{r}$	Position vector	m
SAR	Specific absorption rate	$W\,kg^{-1}$
SAR_{avg}	Spatially averaged specific absorption rate	$W\,kg^{-1}$
t	Time	s
T	Temperature	°C or K
T_a	Arterial blood temperature	°C
T_∞	Ambient temperature	°C
V	Volume	m^3
V_i	Volume of computational cell i	m^3
w_b	Blood mass perfusion rate	$kg\,m^{-3}\,s^{-1}$
α_{earbud}	Effective earbud heat-capacity correction factor	–
ΔT	Temperature increase; subscripts "all", "electronics", and "EM" denote the corresponding heating contributions	°C
ε	Surface emissivity	–
ϵ_r	Relative permittivity	–
ρ	Mass density	$kg\,m^{-3}$
σ	Electrical conductivity	$S\,m^{-1}$
θ	Parameter vector used in the optimization	–

Abbreviations

Abbreviation	Definition
ABS	Acrylonitrile–butadiene–styrene
CSF	Cerebrospinal fluid
CST	CST Studio Suite
EM	Electromagnetic
FIT	Finite integration technique
GAMG	Geometric-algebraic multi-grid
ICNIRP	International Commission on Non-Ionizing Radiation Protection
IEEE	Institute of Electrical and Electronics Engineers
IR	Infrared
ISM	Industrial, Scientific, and Medical
OAT	One-at-a-time
RF	Radiofrequency
RMSE	Root-mean-square error
RMS	Root mean square
ROI	Region of interest
SIMPLE	Semi-Implicit Method for Pressure-Linked Equations

(International Commission on Non-Ionizing Radiation Protection (ICNIRP), 2020). Reliable prediction of the associated thermal response therefore remains an important aspect of exposure assessment, and current protection frameworks rely on dosimetric quantities such as SAR and, at higher frequencies, absorbed power density to relate electromagnetic exposure to potential thermal effects (Health Protection Agency (HPA), 2012; Scientific Committee on Emerging and Newly Identified Health Risks (SCENIHR), 2015; Hirata et al., 2021). Within the present 2.3–2.45 GHz frequency range, local SAR is therefore the relevant exposure quantity, while temperature increase provides the corresponding thermal-response metric.

Bluetooth technology operates in the 2.4 GHz to 2.48 GHz Industrial, Scientific, and Medical (ISM) band and is widely used for short-range wireless communication between devices such as headphones, mobile phones, hands-free kits, and car systems. These devices generally operate at relatively low power levels, ranging from a few milliwatts up to approximately 100 mW (Bluetooth Special Interest Group, 2021). Nevertheless, Bluetooth headphones and earbuds have become widely used in recent years, often for prolonged periods of time, which has contributed to growing interest in accurately characterizing their near-body electromagnetic and thermal behavior.

Compared with conventional mobile-phone exposure, wireless earbuds represent a distinct exposure scenario because they operate directly in or near the ear, where the device is positioned close to superficial tissues and partially confined by the surrounding anatomy (Kim et al., 2024). In this configuration, local temperature elevation may arise from two concurrent mechanisms: electromagnetic energy absorption in tissue and self-heating of the device caused by internal electronic power deposition (Bauer et al., 2018, 2019). While electromagnetic absorption is associated with wireless transmission, device self-heating can be represented as an additional heat source associated with internal power dissipation (Yun et al., 2023). As wearable devices continue to become smaller and more power-dense, understanding the combined thermal impact of these mechanisms is becoming increasingly important for device design, user comfort, and exposure assessment (Yun et al., 2023).

A substantial body of previous research has examined radiofrequency dosimetry in the human head and demonstrated that devices positioned near the ear can produce highly localized electric-field and SAR distributions (Vidjak et al., 2025; Christopher et al., 2021; Wake et al., 2009; Cardis et al., 2008). In parallel, bioheat transfer modeling based on the Pennes formulation (Pennes, 1948) has long been used to predict temperature evolution in biological tissue subjected to internal or external heat sources (Hristov, 2019; Etehadtavakol and Ng, 2020). However, electromagnetic exposure assessment and bioheat modeling are often addressed as separate steps. Electromagnetic analyses commonly emphasize exposure quantities such as SAR, whereas thermal analyses require corresponding heat-source terms to estimate the resulting temperature response.

A recent review of three-dimensional human thermoregulation models highlighted the ability of anatomically realistic models to predict temperature distributions at tissue and organ levels (Xu et al., 2023). In head-and-neck thermal modeling, predicted temperatures have also been shown to depend on the adopted tissue model, blood perfusion, and thermal conductivity, with model performance assessed against measured treatment-power data (Drizdal et al., 2023).

Recent theoretical studies have extended classical heat-transfer formulations by incorporating phase-lag, memory-dependent, thermoelastic, and electromagnetic effects. These approaches have been applied to skin tissue subjected to thermal loading (Megahid, 2025; Salem et al., 2024), combined electromagnetic and thermal loading (Megahid, 2026a), and laser irradiation (Megahid, 2026c). Related formulations have also been investigated more broadly in magneto-poroelastic media (Megahid, 2026b), semiconductor systems (Khan et al., 2026), and double-porosity thermoelastic solids (Ailawalia et al., 2025). Such studies provide insight into non-Fourier, memory-dependent, and coupled

thermomechanical responses. The present study addresses a complementary device-specific problem by combining experimentally identified earbud heat generation, near-field electromagnetic absorption, and a three-dimensional anatomical Pennes bioheat model.

From a modeling perspective, electromagnetic–thermal analysis represents a multiphysics problem in which distinct physical fields are linked through energy deposition. When the temperature rise does not significantly alter the electromagnetic properties of tissue, the problem can be treated sequentially: the electromagnetic field is solved first, the resulting absorbed power distribution is determined, and this information is then introduced into the bioheat model as a thermal source term. This separation motivates a coupled approach in which spatially resolved electromagnetic power deposition and experimentally estimated device heat generation are incorporated within the same anatomically resolved bioheat model.

Recent electromagnetic–thermal dosimetry studies have increasingly focused on linking localized temperature elevation to absorbed high-frequency electromagnetic energy in biological tissue. In particular, recent work associated with IEEE ICES TC95 Subcommittee 6 has examined dosimetric and thermal quantities across tissue configurations ranging from canonical planar models to anatomically realistic human models (Li et al., 2021, 2023, 2024, 2026). These studies reinforce the importance of integrated electromagnetic–thermal workflows while also highlighting the need for application-specific investigations of compact wearable devices operating near sensitive anatomical regions.

The present study addresses this gap by developing an integrated framework for predicting the localized bioheat response of the human head to a wireless earbud device. The framework combines infrared thermography measurements performed on a tissue-mimicking ear phantom, inverse identification of effective thermal parameters, full-wave electromagnetic simulations of a representative earbud antenna initially designed for the 2.45 GHz ISM band and evaluated at its tissue-loaded resonance near 2.3 GHz, and three-dimensional bioheat analysis in an anatomically realistic human head model. Within this workflow, electromagnetic field distributions are used to calculate spatially resolved SAR, which is subsequently incorporated into the bioheat model as a volumetric heat source. In parallel, controlled thermal measurements are used to estimate effective device-related heat generation associated with earbud operation under confined in-ear conditions.

The main contribution of this work is the establishment of a practical coupled CST-to-OpenFOAM (Dassault Systèmes, 2025; OpenFOAM Foundation, 2023) workflow for near-head wearable devices. Accordingly, the overarching objective is to quantify, within the same anatomical thermal model, the relative temperature contributions of electromagnetic tissue absorption and earbud self-heating.

The study combines an effective electronics heat source identified using a reduced earbud–phantom thermal calibration model with SAR derived from a geometrically realistic near-ear electromagnetic model within an anatomically resolved head bioheat model. This framework enables direct comparison between heating caused by electromagnetic absorption and heating originating from the earbud electronics. In addition, the work investigates the influence of blood perfusion, tissue thermal conductivity, and SAR averaging strategies on the predicted thermal response. By linking experimental measurements, electromagnetic simulation, and bioheat modeling within a single computational framework, the proposed methodology provides a practical basis for design-stage evaluation and preliminary thermal assessment of next-generation wearable wireless devices.

The remainder of this paper is organized as follows. Section 2 presents the methodology, including the coupled electromagnetic–thermal workflow, electromagnetic simulations, bioheat model, and experimental parameter-identification procedure. Section 3 presents the results and discussion, including electromagnetic field distributions, SAR analysis, and predicted temperature response of the head model. Finally, Section 4 summarizes the main findings and conclusions.

2. Methods

2.1. Coupled workflow

The overall workflow combines both experimental and computational approaches. First, EM field simulations are performed for a representative wireless earbud placed within the ear, yielding spatial distributions of the electric field that are subsequently used to calculate the SAR.

Next, the resulting EM power deposition is translated into equivalent volumetric heat sources for use in thermal modeling. In parallel, targeted IR thermography measurements are conducted on a tissue-mimicking ear phantom. These experiments are coupled with inverse heat-transfer analysis to determine effective thermal properties and to estimate device-related heat generation under confined in-ear conditions.

Finally, steady-state bioheat simulations are carried out using an anatomically realistic three-dimensional human head model, which incorporates tissue-specific thermophysical and physiological characteristics. The experimentally derived parameters, together with the simulated EM field data, are integrated into the bioheat solver to facilitate a coupled EM–thermal assessment of temperature elevation in head tissues.

2.2. Electromagnetic model

The interaction between EM waves and biological tissue is governed by Maxwell's equations, which were solved numerically in this study to obtain the spatial distribution of the electric field in and around the ear region. These field solutions form the basis for quantifying EM exposure through the SAR, defined as the rate of EM energy per unit mass of tissue.

Therefore, at the local level, for time-harmonic dependence, SAR, representing absorbed power per unit tissue mass, i.e. the ratio of differential power P dissipated in a differential tissue mass m, can be expressed as (Razek, 2023; International Commission on Non-Ionizing Radiation Protection (ICNIRP), 2020):

$$\mathrm{SAR} = \frac{\mathrm{d}P}{\mathrm{d}m} = \frac{\frac{1}{2}\sigma|\vec{E}|^2\,\mathrm{d}V}{\rho\,\mathrm{d}V} = \frac{\sigma|\vec{E}|^2}{2\rho}, \tag{1}$$

where σ denotes the electrical conductivity of the tissue, ρ its mass density, and $|\vec{E}|$ is the magnitude, i.e. the peak value, of the electric field.

For the case of root mean square (r.m.s.) values, the factor $1/2$ is omitted. Furthermore, in the case of fast adiabatic heat generation the SAR is directly proportional to the local temperature increase:

$$\mathrm{SAR} = c_\mathrm{p}\frac{\mathrm{d}T}{\mathrm{d}t}, \tag{2}$$

where T stands for temperature, t is time, and c_p denotes specific heat capacity.

Since the electric field can vary over small spatial scales, regulatory exposure limits are not defined using pointwise SAR, but rather through spatially averaged quantities. Accordingly, SAR is evaluated over a prescribed tissue mass. In the present study, both 1 g and 10 g spatially averaged SAR are considered for dosimetric comparison, while current ICNIRP and IEEE exposure frameworks specify local SAR averaging over 10 g of tissue (International Commission on Non-Ionizing Radiation Protection (ICNIRP), 2020; IEEE, 2019). The corresponding averaged SAR is given by (International Commission on Non-Ionizing Radiation Protection (ICNIRP), 2020):

$$\mathrm{SAR}_\mathrm{avg} = \frac{\mathrm{d}P}{\mathrm{d}m} = \frac{\int_V \sigma|\vec{E}|^2\,\mathrm{d}V}{2\int_V \rho\,\mathrm{d}V}, \tag{3}$$

where V represents the volume associated with the selected averaging mass. The resulting SAR distribution is subsequently used to assess

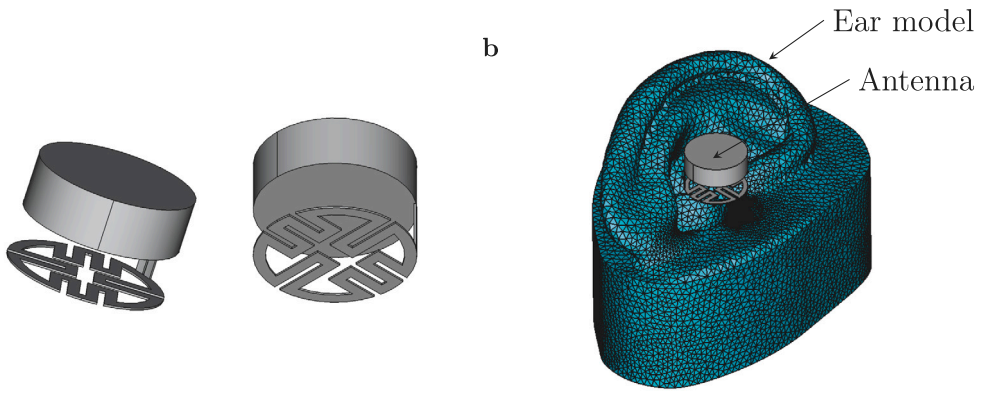


Fig. 1. Electromagnetic model used for the earbud exposure analysis. a, Bent-loop antenna geometry shown from different perspectives and representative of Bluetooth earbud antenna designs. b, Position of the bent-loop antenna relative to the homogeneous human-ear model, with the radiating section directed toward the tissue.

thermally induced effects in tissue. For the case of constant tissue within the volume, the averaged SAR expression can also be written as:

$$\mathrm{SAR}_{\mathrm{avg}} = \frac{\int_V \mathrm{SAR}\,\mathrm{d}V}{V}. \tag{4}$$

The EM model was constructed using a realistic ear geometry combined with a bent-loop antenna, shown from different perspectives in Fig. 1a, representative of designs reported for Bluetooth earbuds (Woo and Joong Yoon, 2021). The antenna was initially designed for operation at 2.45 GHz, corresponding to a standard Bluetooth frequency band (Padgette et al., 2022). However, when positioned in close proximity to the ear, the antenna exhibited a shift in its impedance characteristics, with the optimal matching frequency moving to approximately 2.3 GHz. This behavior is attributed to the strong near-field interaction with the surrounding lossy tissue. Accordingly, the 2.3 GHz field distribution was used to characterize the tissue-loaded strong-coupling condition of the uncompensated antenna. This condition is not intended to represent the exact operating state of a commercial Bluetooth antenna matched at 2.45 GHz.

To focus on EM coupling effects while maintaining a controlled modeling environment, the ear tissue was represented as a homogeneous lossy dielectric. The material properties were selected to match those of skin at 2.45 GHz, with relative permittivity $\epsilon_r = 38$, conductivity $\sigma = 1.46\,\mathrm{S\,m^{-1}}$, and density $\rho = 1109\,\mathrm{kg\,m^{-3}}$ (IT'IS Foundation, 2024). In the EM simulations, the base of the ear model was extended to approximately 32 mm in order to reduce artificial signal reflections from the truncated tissue boundary. This extension was selected to be larger than the estimated penetration depth in skin at 2.45 GHz, approximately 22.6 mm, so that the fields were sufficiently attenuated before reaching the lower boundary of the model.

The antenna structure was modeled as a perfect electric conductor and placed above the ear concha, as illustrated in Fig. 1b, with its radiating section directed toward the tissue to emulate a representative high-exposure configuration. Due to the complex geometry of the ear surface, the separation between the antenna and tissue was not constant, varying between 6.9 and 7.6 mm. The antenna was excited using a discrete port with a forward feed power of 10 mW, while the accepted power depended on the frequency-dependent antenna matching.

For the subsequent thermal analysis, it was necessary to define EM exposure in regions of the head outside the immediate vicinity of the earbud. Rather than extending the detailed near-field EM simulation to the entire head, a simplified approach was adopted in which a uniform background electric field was extracted from the EM solution at a point located 22.6 mm inward from the ear surface position exhibiting the peak electric-field magnitude.

The resulting value, $|E| = 5.06\,\mathrm{V\,m^{-1}}$, was then applied uniformly throughout the rest of the head model. This approximation preserves a realistic level of background EM loading while limiting the computational complexity of the coupled EM–thermal problem. This uniform value is intended to represent low-level background loading outside the detailed near-ear domain and should not be interpreted as an exact prediction of the deep-tissue electromagnetic field.

2.2.1. Electromagnetic simulation setup

Electromagnetic simulations were performed using CST Studio Suite® (Dassault Systèmes, Vélizy-Villacoublay, France) (Dassault Systèmes, 2025), employing the time-domain solver based on the finite integration technique (FIT) formulation of Maxwell's curl equations.

The antenna response and field characteristics were analyzed over the frequency range from 0 to 5 GHz using 1001 uniformly spaced sampling points. Based on the resulting frequency response, the operating condition of interest was identified at 2.3 GHz, and the corresponding electric-field distribution was extracted for use in the subsequent thermal simulations.

The computational domain was discretized using a hexahedral mesh, with targeted local refinement applied in regions of high field variation, particularly near the antenna structure and at the ear–air interface, in order to accurately capture near-field effects.

2.3. Bioheat model

Heat transfer within biological tissue is described using the Pennes bioheat formulation (Pennes, 1948), with additional source terms to incorporate electromagnetic energy deposition and heat generated by the wireless earbud during operation. The resulting governing equation can be written as (Pennes, 1948):

$$\begin{aligned}\rho(\vec{r})c_{\mathrm{p}}(\vec{r})\frac{\partial T(\vec{r},t)}{\partial t} &= \nabla\cdot(k(\vec{r})\nabla T(\vec{r},t)) \\ &+ c_{\mathrm{p,b}}(\vec{r})\omega_{\mathrm{b}}(\vec{r})(T_{\mathrm{a}} - T(\vec{r},t)) + q_{\mathrm{m}}(\vec{r}) + \rho(\vec{r})\,\mathrm{SAR}(\vec{r}) + q_{\mathrm{ext}}(\vec{r}),\end{aligned} \tag{5}$$

Here, $T(\vec{r},t)$ denotes the local tissue temperature at position $\vec{r}$ and time t. The parameters ρ, c_{p}, and k correspond to tissue density, specific heat capacity, and thermal conductivity, respectively. The parameters $c_{\mathrm{p,b}}$ and ω_{b} denote the specific heat capacity of blood and the blood mass perfusion rate, respectively, while T_{a} is the arterial blood temperature. Metabolic heat generation is described by q_{m}. The term $\rho\,\mathrm{SAR}$ accounts for volumetric heating due to EM energy absorption, whereas q_{ext} is used to account for nonelectromagnetic heat sources arising from the earbud's internal electronic components.

2.3.1. Human head model

The computational domain is based on a three-dimensional anatomically realistic human head model (Noetscher et al., 2014), within which the earbud is positioned inside the ear canal. The external

Table 1
Thermophysical, physiological, and electrical properties considered in the bioheat simulations (Noetscher et al., 2014; Thermtest Inc., 2024; IT'IS Foundation, 2024).

Material	ρ (kg m^{-3})	c_p (J kg^{-1} K^{-1})	k (W m^{-1} K^{-1})	σ (S m^{-1})	w_b (kg m^{-3} s^{-1})	q_m (W m^{-3})	q_{ext} (W m^{-3})
Soft tissues	1109	3390.5	0.3722	1.46	2.0641	1827	0
Skull	1653	1649.2	0.32	0.53785	0.4915	435	0
CSF, ventricles	1007	4095.5	0.5733	3.46	0	0	0
Gray matter	1044.5	3695.8	0.547	1.81	13.9555	16 230	0
White matter	1041	3582.8	0.481	1.21	3.8673	4498	0
Eye	994.0	3997.0	0.58	3.46	20.1063	22 683	0
Cerebellum	1045	3653	0.506	2.1	14.078	16 373	0
Tongue	1090.4	3421.2	0.4950	1.8	1.4880	1317	0
Jaw	1653	1649.2	0.32	0.53785	0.4915	435	0
Earbud	1040	1506	0.138	0	0	0	0
Electronics	1040	1054.2	0.138	0	0	0	1.05×10^5

geometry of the model, including the skin surface, eye surfaces, and the exposed portion of the earbud, is illustrated in Fig. 2a. A corresponding view of the internal structure is provided in Fig. 2b, where the different tissue compartments and the locations of applied boundary conditions are indicated.

The head model follows the multi-domain anatomical representation reported by Noetscher et al. (2014). It comprises several distinct tissue regions, including the skull, cerebrospinal fluid (CSF), gray matter, white matter, ventricles, cerebellum, eyes, tongue, jaw, and surrounding soft tissues. Each of these regions was treated as homogeneous and assigned constant thermophysical and physiological properties to enable tractable numerical simulations.

The earbud was incorporated into the model as a solid domain occupying the ear canal. Due to the absence of detailed information on the internal geometry of the device, its internal structure was not explicitly resolved. Instead, heat generation associated with electronic components was represented using an effective cylindrical subdomain referred to as the "Electronics" region. This region serves as a surrogate for the combined heat dissipation of the internal electronics rather than representing the physical battery alone. The corresponding heat generation was introduced into the bioheat formulation through the volumetric source term q_{ext}.

The material properties of the earbud enclosure were approximated based on acrylonitrile–butadiene–styrene (ABS), a thermoplastic commonly used in consumer electronic housings. Since the exact material composition and internal construction of the device are not publicly available, literature values for ABS were adopted (Thermtest Inc., 2024). Furthermore, to account for the unresolved internal components such as electronics, adhesives, and internal cavities, the thermal inertia of the earbud was represented using an effective specific heat capacity obtained through experimental parameter identification.

Thermophysical and physiological parameters for all biological tissues were obtained from the IT'IS tissue properties database (IT'IS Foundation, 2024). Electrical properties used for SAR conversion were selected at 2.45 GHz, corresponding to the intended ISM-band design frequency; their use with the field distribution evaluated at 2.3 GHz represents a band-specific approximation over the shifted-resonance condition. The thermal response of the human body is strongly influenced by blood perfusion, particularly within the core thermal compartment, which is highly perfused and can be considered relatively homogeneous. As a result, the core body temperature is tightly regulated and maintained within a narrow range, typically around 37 °C under resting conditions.

Based on these physiological considerations, the arterial blood temperature was assumed to be equal to the core body temperature and was therefore set to $T_a = 37$ °C (Hymczak et al., 2021). This assumption is commonly adopted in bioheat modeling and is justified by the strong thermoregulatory mechanisms that stabilize the core temperature despite localized thermal perturbations. A complete summary of the material properties used in the simulations is provided in Table 1.

2.3.2. Boundary conditions

Thermal boundary conditions were defined to account for heat exchange between the head model, the earbud, and the surrounding environment (Fig. 2b). These conditions govern both external losses and internal heat transfer with the computational domain.

All external surfaces exposed to ambient air – including the skin, the outer surface of the earbud, and the exposed eye regions – were modeled using a convective (Robin-type) boundary condition of the form $\vec{q} \cdot \vec{n} = h(T - T_\infty)$, where h is the effective heat transfer coefficient and T_∞ is the ambient temperature. In practice, heat exchange at the surface occurs both through convection and radiation. Based on reported experimental (De Dear et al., 1997) and numerical (Alali and Eckels, 2024) studies, convective and radiative heat transfer coefficients of 3.6 and 4.1 W m^{-2} K^{-1}, respectively, were combined to yield an effective coefficient of $h = 7.7$ W m^{-2} K^{-1}, which was adopted in this work. The ambient temperature was set to $T_\infty = 20$ °C.

At the truncated base of the head model, representing the interface with the rest of the body, an adiabatic boundary condition was imposed, i.e., $\vec{q} \cdot \vec{n} = 0$. This assumption neglects heat exchange across the truncation plane and isolates the computational domain. In Fig. 2b, this interface is indicated by the dark gray region.

All internal interfaces between different tissue regions, as well as between the earbud and the surrounding tissues, were assumed to be in perfect thermal contact, with both temperature and normal heat flux continuous across the interface, such that $T_i = T_{i+1}$ and $k_i \nabla T_i \cdot \vec{n} = k_{i+1} \nabla T_{i+1} \cdot \vec{n}$, where i and $i+1$ denote adjacent tissue regions, and $\vec{n}$ is the unit normal vector to the interface.

2.3.3. Bioheat simulation setup

A custom bioheat solver was developed within the OpenFOAM v11 framework (OpenFOAM Foundation, 2023) by extending the foamMultiRun architecture, following the methodology of Horvat and Iljaž (2025). The solver was used to compute steady-state temperature distributions based on the bioheat equation, with EM field data mapped from the CST simulations as volumetric heat sources. Simulations were executed on a Linux-based workstation running Linux Mint 22, equipped with an Intel® Core™ i9-10940X CPU (14 cores, 28 threads, 3.30 GHz) and 62 GiB of RAM. Although computations were performed in a single-domain configuration, multi-threaded linear solvers were utilized where available, and results were post-processed using ParaView 5.11.2. The governing equations were solved in steady-state mode using the SIMPLE algorithm. A nominal time loop with a step size of 1 s was employed solely as an iteration-control mechanism and does not represent physical transient integration. The computational mesh consisted of 2,141,995 cells, as determined from the mesh-independence study presented in Section 2.5.1. Convergence was defined by a temperature residual below 10^{-8}. The resulting linear systems were solved using the geometric-algebraic multi-grid (GAMG) solver with Gauss–Seidel smoothing. Each simulation required approximately 228 s of wall-clock time to reach convergence.

The steady-state formulation was selected to determine the asymptotic temperature distribution under continuous source conditions and

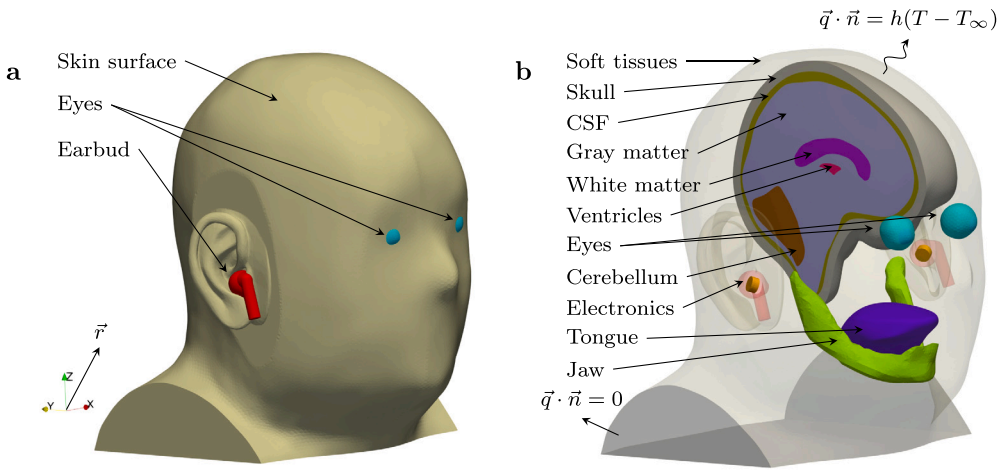


Fig. 2. Anatomical head model and thermal boundary conditions used in the bioheat simulations. a, External view showing the skin surface, exposed eye surfaces, and inserted earbud. b, Internal tissue domains and applied thermal boundary conditions.

to isolate the relative contributions of device self-heating and electromagnetic absorption without introducing an assumed communication duty cycle. The transient phantom model was used for parameter identification, whereas transient anatomical simulations are reserved for future work involving realistic time-dependent power histories.

2.4. Thermal measurements and parameter identification

2.4.1. Measurement setup and procedure

Thermal measurements were conducted to characterize the heating behavior of the wireless earbud under controlled operating conditions and to provide temperature data for subsequent parameter identification. A tissue-mimicking ear phantom fabricated from ballistic gelatin was used as the measurement medium because of its high water content and its thermal behavior being reasonably representative of soft biological tissue (Winter and Shifler, 1975). The geometry of the earbud and the ear phantom with its characteristic dimensions, including their relative positioning, is illustrated in Fig. 3a and b, respectively.

The ear phantom was embedded in a carved styrofoam support that provided both mechanical stability and thermal insulation on the rear and lateral sides. The interface between the phantom and the support was sealed to minimize air gaps and suppress parasitic convective heat transfer. The complete measurement arrangement, including the earbud–ear assembly, support structure, and infrared camera, is shown in Fig. 3c, where the characteristic dimensions of the setup are indicated.

Infrared thermography was used to record the transient surface temperature. Measurements were performed using a FLIR A655sc infrared camera (FLIR, 2025), mounted on a fixed tripod at a distance of approximately 55 cm from the phantom (see Fig. 3c). The camera is equipped with a 640 × 480 uncooled microbolometer detector and provides a thermal sensitivity better than 30 mK. The manufacturer specifies an absolute measurement accuracy of ±2 °C or ±2% of the reading. The present analysis used a same-frame ambient-referenced temperature difference, which reduces common-mode camera drift and slow ambient variation. The emissivity of the surface was set to $\varepsilon = 0.95$.

The finalized measurement configuration is shown in Fig. 3d. It consists of three elements within the camera field of view: (1) the ballistic ear phantom with the inserted earbud, (2) a standalone ballistic ear serving as a control reference, and (3) a black reference block used to monitor ambient temperature. The earbud was positioned in the phantom to approximate realistic in-ear placement, ensuring consistent contact conditions between the device and the surrounding surface.

All measurements were conducted in a temperature-controlled cleanroom maintained at approximately 23.5 °C. The environment was selected to minimize external disturbances such as air drafts, temperature fluctuations, and radiative interference from surrounding equipment. These controlled conditions ensured that the observed temperature changes were primarily driven by heat generated within the earbud.

Two operating conditions were investigated. In the “Idle” state, the earbud was powered on without transmitting audio, representing a low-power baseline. In the “Playback” state, broadband white noise was continuously played for 60 min, corresponding to active operation. This heating phase was followed by a passive cooling period of approximately 80 min, allowing characterization of both the transient heating and cooling response of the system.

Thermal images were recorded continuously at a sampling rate of 2 Hz over the full measurement duration. Each operating condition was repeated three times under identical conditions to ensure reproducibility. Prior to each run, the system was returned to a comparable initial state, and care was taken to maintain consistent earbud placement and camera alignment.

Temperature evaluation was performed using regions of interest (ROIs) defined on the infrared image. A first ROI was placed on the visible outer surface of the earbud, while a second ROI was defined on the ambient reference block. The temperature rise induced by the device was expressed as the ambient-referenced temperature:

$$\Delta T(t) = T_{\text{earbud}}(t) - T_{\text{ambient}}(t), \tag{6}$$

where $T_{\text{earbud}}(t)$ and T_{ambient} denote the spatially averaged temperatures within the respective ROIs. This differential formulation reduces the influence of slow ambient temperature drift and provides a robust measure of device-induced heating.

For each scenario, the recorded temperature–time curves were temporally aligned and averaged across repetitions to obtain a representative mean response. The resulting $\Delta T(t)$ data served as the primary experimental observable for the subsequent identification of effective thermal parameters in the simplified earbud model.

2.4.2. Thermal model and optimization procedure

To interpret the measured temperature evolution in terms of effective device-level thermal properties, a simplified numerical model of the earbud–phantom assembly was constructed. The purpose of this model was to capture the dominant mechanisms governing heat generation, storage, and dissipation during the thermal measurements. In this way, the model serves as an intermediate calibration tool linking the infrared thermography data to the parameters later used in the anatomical bioheat simulations.

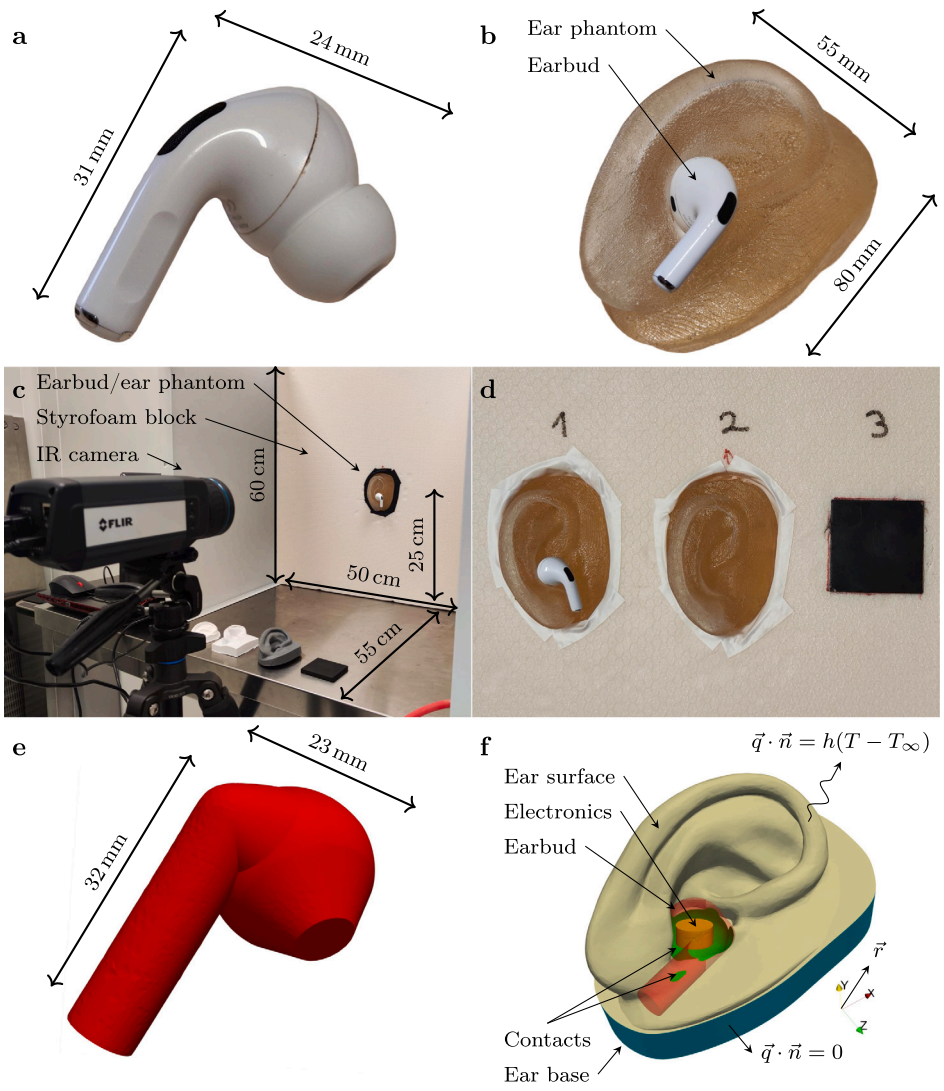


Fig. 3. Experimental configuration and simplified thermal calibration model used to identify the effective earbud-heating parameters. a, Commercial earbud with characteristic dimensions. b, Ballistic-gelatin ear phantom with the inserted earbud and characteristic dimensions. c, Full infrared-thermography measurement arrangement, including the earbud–phantom assembly, styrofoam support, and infrared camera. d, Final camera field of view containing the earbud–phantom assembly, the standalone control phantom, and the ambient reference block. e, Reduced-order earbud geometry with characteristic dimensions. f, Computational earbud–phantom assembly showing the effective electronics region and applied thermal boundary conditions.

The simplified computational representation is shown in Fig. 3e and f. Fig. 3e presents the reduced-order earbud geometry with its characteristic dimensions, while Fig. 3f shows the complete ear–earbud assembly used for the thermal analysis. The model includes the outer ear surface, the supporting phantom base, the earbud casing, and an internal earbud subdomain representing the effective electronics region. Fine structural details that are not expected to significantly affect the macroscopic thermal response were omitted in order to obtain a numerically robust and computationally efficient parametrization model.

Heat transfer in the solid regions was described using the transient heat-conduction equation:

$$\rho(\vec{r})c_p(\vec{r})\frac{\partial T(\vec{r},t)}{\partial t} = \nabla \cdot (k(\vec{r})\nabla T(\vec{r},t)) + q_{ext}(\vec{r}). \quad (7)$$

The source term q_{ext} was applied only within the internal earbud subdomain denoted as "Electronics" and represents the effective heat released by the electronic components during operation. Outside this region, $q_{ext} = 0$ was prescribed. The thermophysical properties assigned to the "Ear phantom", "Earbud", and "Electronics" subdomains are summarized in Table 2.

Table 2
Initial thermophysical properties and external heat-generation terms used in the simplified earbud–phantom thermal calibration model (Noetscher et al., 2014; Thermtest Inc., 2024; Winter and Shifler, 1975).

Material	ρ (kg m^{-3})	c_p (J kg^{-1} K^{-1})	k (W m^{-1} K^{-1})	q_{ext} (W m^{-3})
Ear phantom	1063	2679.55	0.356	0
Earbud	1040	1506	0.138	0
Electronics	1040	1506	0.138	9.0×10^4

The thermal boundary conditions were chosen to reproduce the experimental measurement situation, as shown in Fig. 3f. A convective boundary condition was imposed on the exposed surfaces of both the earbud and the ear phantom, $\vec{q} \cdot \vec{n} = h(T - T_\infty)$. At the "Ear base", an adiabatic condition, $\vec{q} \cdot \vec{n} = 0$, was imposed to represent the thermally insulating effect of the supporting structure. Perfect thermal contact, i.e., $T_i = T_{i+1}$ and $k_i \nabla T_i \cdot \vec{n} = k_{i+1} \nabla T_{i+1} \cdot \vec{n}$, was assumed at the earbud–phantom interface, allowing conductive heat transfer across the contacting surfaces without additional interfacial resistance.

Parameter identification was carried out by matching the numerical solution to the measured ambient-referenced temperature increase

$\Delta T(t)$ defined in the measurement procedure. This ensured that the model was calibrated directly against the device-induced temperature rise while reducing sensitivity to slow ambient drift.

The unknown model parameters were determined through bounded nonlinear least-squares optimization. The optimized parameter set was defined as $\theta = \{q_{ext}, h, \alpha_{earbud}\}$, where α_{earbud} is a correction factor for the effective heat capacity of the simplified earbud shell, which was introduced as $\alpha_{earbud} = c_{p,earbud}/c_{p,ABS}$, where $c_{p,ABS}$ is the nominal specific heat capacity of ABS and $c_{p,earbud}$ is the effective value used in the calibration model. This correction accounts for the fact that the real earbud is a composite structure containing internal components, cavities, adhesives, and interfaces that alter its apparent thermal storage behavior compared with a homogeneous solid.

The objective function was defined as:

$$J(\theta) = \frac{1}{2}\sum_{i=1}^{N}\left[\Delta T_{sim}(t_i;\theta) - \Delta T_{meas}(t_i)\right]^2, \tag{8}$$

where $\Delta T_{sim}(t_i;\theta)$ and $\Delta T_{meas}(t_i)$ denote the simulated and measured temperature increases, respectively. The minimization was performed using custom Python scripts that called the bounded Trust–Region Reflective least-squares routine implemented in SciPy (Virtanen et al., 2020), which is well suited for nonlinear parameter estimation problems with physically constrained parameters.

To reduce parameter correlation, the identification was performed in two sequential steps. First, the effective heat-generation rate q_{ext} and the heat transfer coefficient h were identified from quasi-steady portions of the measured response. For this step, the objective function was evaluated over the windows $t = 3050$ s to 3550 s and $t = 7900$ s to 8400 s. These intervals correspond to the near-plateau region close to the end of the playback phase and the late cooling response, respectively. Second, with q_{ext} and h at their optimized values, the heat-capacity correction factor α_{earbud} was identified from the transient portions of the curve using the windows $t = 60$ s to 900 s and $t = 3660$ s to 4500 s. These intervals capture the initial heating and early cooling behavior, where the thermal inertia of the earbud–phantom system has the strongest influence. The full measurement sequence consisted of a 3600 s active playback phase followed by a 4850 s passive cooling phase.

Physically motivated lower and upper bounds were imposed on all fitted quantities in order to ensure realistic parameter values and stable convergence:

$$\begin{aligned} 6.0\times10^4 \le q_{ext} \le 1.2\times10^5 \quad & \mathrm{W\,m^{-3}}, \\ 3.0 \le h \le 12.0 \quad & \mathrm{W\,m^{-2}\,K^{-1}}, \\ 0.70 \le \alpha_{earbud} \le 1.30. & \end{aligned} \tag{9}$$

The starting values were $q_{ext} = 9.0\times10^4\ \mathrm{W\,m^{-3}}$, $h = 7.7\ \mathrm{W\,m^{-2}\,K^{-1}}$, and $\alpha_{earbud} = 1.0$. Convergence was assessed from the reduction of the objective function, the stability of the optimized parameters between successive iterations, and the agreement between the simulated and measured temperature–time curves.

The optimized parameters provide a compact thermal description of the earbud under the controlled phantom measurement conditions. Since the same effective electronics volume was used in the calibration model and in the anatomical head model, the optimized volumetric source term q_{ext} was transferred directly without rescaling. The fitted coefficient h was retained only for reproducing the phantom experiment, because the external heat-transfer conditions depend on the specific geometry, exposed surface area, local airflow, ambient conditions, and support configuration. The fitted heat-capacity correction factor α_{earbud} was used to determine the effective specific heat capacity $c_{p,earbud}$ required to reproduce the transient thermography response of the simplified earbud model; however, because the head simulations in this study were performed in steady state, this parameter does not affect the final steady-state temperature field.

2.4.3. Identified thermal parameters

The infrared measurements described above provided the temperature increase referenced to the ambient temperature $\Delta T(t)$ used for parameter identification. Fig. 4a shows a representative infrared temperature map acquired during the experiment, with ROI 1 placed over the heated earbud region and ROI 2 placed on a nearby ambient reference region. The temperature difference between these regions was used to obtain the ambient-referenced temperature rise. Fig. 4b compares the resulting measured temperature response with the optimized numerical prediction over the complete heating and cooling sequence.

Application of the optimization framework yielded a physically consistent parameter set summarized in Table 3. The identified volumetric heat source was $q_{ext} = 1.05\times10^5\ \mathrm{W\,m^{-3}}$. The effective electronics-region volume was $V_{electronics} = 3.93\times10^{-7}\ \mathrm{m^3}$, so the identified volumetric source corresponds to a total effective heat-release rate of $P_{electronics} = q_{ext}\,V_{electronics} = 0.0413\ \mathrm{W} \approx 41.3\ \mathrm{mW}$.

As shown in Fig. 4b, this source term reproduces the measured temperature rise during the active playback phase and gives a near-plateau temperature increase of approximately 2.6 °C before playback stops. Since the same effective electronics volume was used in both the calibration model and the anatomical head model, this volumetric source term was applied directly in the "Electronics" region of the earbud in the subsequent bioheat simulations.

The optimized effective heat-transfer coefficient was $h = 5.67\ \mathrm{W\,m^{-2}\,K^{-1}}$. This value lies within the expected range for natural convection in quiescent air around small bodies, but it should be interpreted as an experiment-specific effective coefficient for the earbud–phantom configuration. The cooling part of Fig. 4b, following the playback stop at $t = 3600$ s, is particularly sensitive to this effective heat-loss coefficient and shows that the optimized model captures the overall decay of the measured temperature rise. For this reason, h was used only in the calibration model.

The effective specific heat capacity of the simplified earbud shell was identified as $c_{p,earbud} = 1054\ \mathrm{J\,kg^{-1}\,K^{-1}}$. This value corresponds to $\alpha_{earbud} = 0.70$ when normalized by the nominal ABS value $c_{p,ABS} = 1506\ \mathrm{J\,kg^{-1}\,K^{-1}}$. The reduction relative to the nominal ABS value is physically plausible, since the real earbud is not a homogeneous solid body but contains internal voids, thin walls, electronic components, adhesive layers, and air-filled layers. These unresolved features reduce the apparent thermal storage of the simplified model and are therefore represented through the effective value $c_{p,earbud}$.

Over the complete heating and cooling sequence, comparison with the mean of three experimental measurements yielded an RMSE of 0.188 °C and a maximum absolute deviation of 0.796 °C. The RMSE normalized by the maximum measured temperature increase of 2.609 °C was 7.21%, indicating reasonable overall agreement between the calibrated simulation and the measured thermal response. The largest deviation occurred shortly after playback termination, during the transition from heating to cooling.

2.5. Verification and cases

2.5.1. Mesh independence study

A mesh-sensitivity assessment was performed for the electromagnetic model. The CST time-domain FIT solver employed a global mesh setting of 20 cells per wavelength, with additional local refinement of the antenna using an edge refinement factor of 12. Convergence was evaluated by monitoring the absorbed power in the tissue ("volume loss in skin") between successive mesh passes. The relative change in absorbed power between successive passes was approximately 2.9%, supporting adequate mesh resolution for the electromagnetic analysis.

For the bioheat model, a mesh-independence study was conducted using three mesh resolutions: coarse, medium and fine. The coarse mesh consists of 1,752,453 cells, the medium mesh 2,141,995 cells, and the fine mesh 10,341,701 cells.

Table 3
Identified effective thermal parameters obtained from the earbud–phantom calibration experiment.

Parameter	Description	Identified value	Use in subsequent model
q_{ext}	Volumetric heat source	1.05×10^5 W m^{-3}	Applied in the electronics region
h	Effective heat-transfer coefficient	5.67 W m^{-2} K^{-1}	Calibration model only
$c_{p,earbud}$	Effective earbud heat capacity	1054 J kg^{-1} K^{-1}	Used for transient calibration

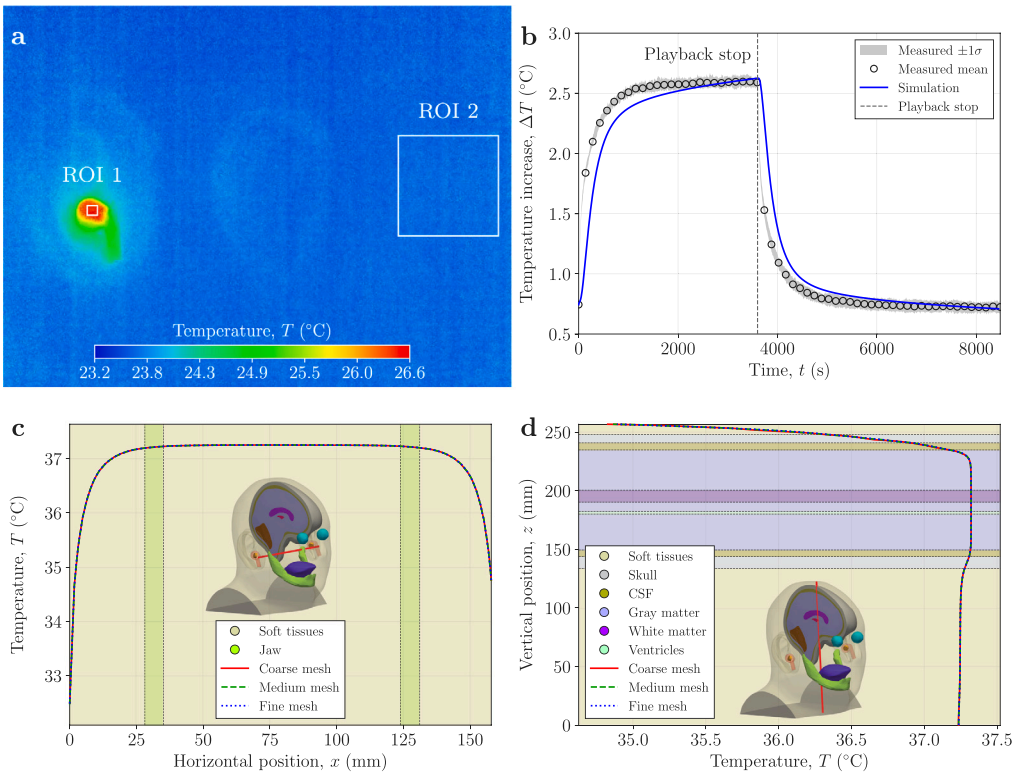


Fig. 4. Experimental calibration and mesh-independence verification of the thermal model. a, Representative infrared temperature map with ROI 1 positioned on the earbud and ROI 2 positioned on the ambient reference region. b, Comparison of the measured and simulated ambient-referenced temperature increase, $\Delta T(t)$, obtained using the optimized earbud–phantom thermal model; the shaded band represents the measured mean $\Delta T(t) \pm 1\sigma$, where σ is the standard deviation of the post-processed ambient-referenced temperature signal. c, Horizontal temperature profiles obtained with the coarse, medium, and fine bioheat meshes along a line passing through the region of maximum heating. d, Vertical temperature profiles obtained with the same mesh resolutions along the head mid-plane; the colored bands in panels c and d indicate the different tissue regions.

The study was performed by comparing temperature profiles obtained with each mesh, as shown in Fig. 4c and d, where Fig. 4c presents the horizontal profile and Fig. 4d the vertical profile. The different regions of the head are color-coded consistently with Fig. 2b. The coarse, medium and fine meshes are represented by solid red, dashed green, and dotted blue lines, respectively.

The horizontal profile is taken along a line passing through the location of maximum heating – resulting from both the earbud electronics and EM exposure – and extends across the head. The vertical profile is taken through the mid-plane of the head, from bottom to top, and is perpendicular to the horizontal line.

In both profiles, the temperature within the interior regions remains slightly above 37 °C, reflecting the prescribed core body conditions imposed via the Pennes perfusion term, along with contributions from metabolic heat generation and other sources. Near the surface, the temperature decreases due to the applied convective boundary condition.

Comparison of the three mesh resolutions shows negligible differences in the temperature distribution for both profiles, indicating mesh-independent results. Nevertheless, the medium mesh was selected for subsequent simulations, as it provides sufficient resolution – particularly near the surface – while maintaining a reasonable computational cost.

2.5.2. Physiological-parameter sensitivity analysis

A local one-at-a-time sensitivity analysis was performed to evaluate the influence of blood mass perfusion and tissue thermal conductivity on the predicted steady-state temperature field. Relative to the baseline case, all nonzero blood mass perfusion rates in the biological tissue regions were decreased and increased by 20%. In separate simulations, the thermal conductivities of all biological tissue regions were decreased and increased by 10%. Only one parameter group was varied in each simulation, while all other material properties, heat-source terms, boundary conditions, geometry, mesh and numerical settings were retained at their baseline values. Sensitivity was evaluated at the location of the maximum total device-induced temperature increase in the baseline simulation, defined from the difference between the fully coupled and bioheat-only temperature fields.

3. Results and discussion

3.1. Electromagnetic field and SAR distributions

Fig. 5a shows the spatial distribution of the electric-field magnitude, $|E|$, near the external ear. The field is highly non-uniform, with a pronounced maximum of $|E|_{max} = 365.25$ V m^{-1} localized within a recessed region near the ear opening. The high-field region is spatially

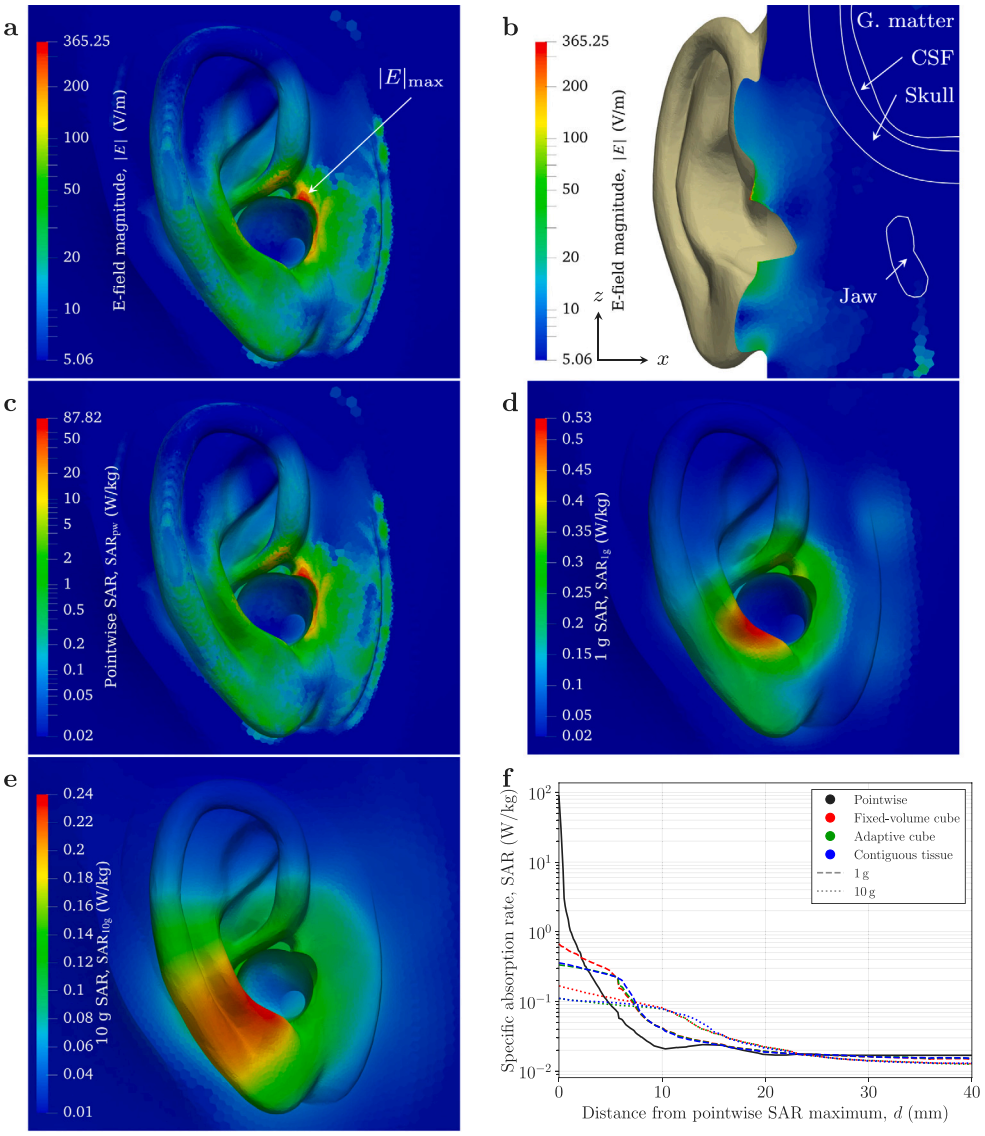


Fig. 5. Spatial distributions of electric-field magnitude and specific absorption rate around the ear, together with the influence of spatial averaging. a, External distribution of electric-field magnitude, showing the localized maximum near the ear opening. b, Electric-field distribution in the x–z cross-section through the pointwise SAR maximum; the white contours indicate material boundaries. c, Pointwise SAR distribution. d, Contiguous-tissue 1 g averaged SAR distribution. e, Contiguous-tissue 10 g averaged SAR distribution. f, SAR profiles evaluated from the pointwise SAR maximum, comparing pointwise SAR with the 1 g and 10 g results obtained using the fixed-volume-cube, adaptive-cube, and contiguous-tissue averaging approaches.

confined, and the field decreases rapidly away from the earbud–tissue interface.

Fig. 5b presents the corresponding x–z cross-section through the pointwise SAR maximum. Because the homogeneous ear model was assigned constant electrical conductivity, σ, and mass density, ρ, the maximum electric-field magnitude coincides with $\mathrm{SAR}_{\mathrm{pw,max}}$. The cross-sectional view demonstrates the rapid spatial decay of the field away from this localized region, while the white contours delineate the material boundaries within the model.

The pointwise and spatially averaged SAR distributions are compared in Fig. 5c–e. Fig. 5c shows the strongly localized pointwise SAR distribution, characterized by a sharp maximum and rapid decay away from the hotspot. Fig. 5d and e show the contiguous-tissue 1 g and 10 g averaged SAR distributions, respectively. Spatial averaging substantially reduces the peak value and produces a smoother, more extended distribution. This effect is more pronounced for the 10 g averaging mass, while the location of the maximum also shifts relative to the pointwise hotspot. Nevertheless, the highest SAR values remain concentrated within the same general near-ear region. The influence of the averaging procedure on the peak values and their spatial locations is examined in the following subsection.

3.2. Influence of SAR averaging strategy

To evaluate the influence of the SAR averaging procedure, pointwise SAR was compared with fixed-volume-cube, adaptive-cube, and contiguous-tissue averaging approaches. The pointwise SAR was retained as the local electromagnetic heat source in the bioheat simulations, whereas the averaged SAR quantities were evaluated only for dosimetric comparison.

For the averaged quantities, the local SAR values were mass-weighted over the selected tissue cells according to:

$$\mathrm{SAR}_{\mathrm{avg}} = \frac{\sum_i \mathrm{SAR}_i\, m_i}{\sum_i m_i}, \qquad m_i = \rho_i V_i. \tag{10}$$

Only biological tissue cells were included in the averaging pool. In the fixed-volume-cube approach, an axis-aligned cube was centered at each cell centroid. Cube side lengths of 10 mm and 21.54 mm were

Table 4
Comparison of SAR evaluation approaches used to assess the influence of spatial averaging on peak SAR values and locations.

Averaging mass	SAR evaluation method	SAR_{max} ($W\,kg^{-1}$)	$d_{SAR_{pw,max}}$ (mm)
–	Pointwise SAR	87.8174	0
1 g	Fixed-volume cube	0.7274	0.68
	Adaptive cube	0.5529	17.50
	Contiguous tissue	0.5347	18.13
10 g	Fixed-volume cube	0.3877	17.33
	Adaptive cube	0.2343	19.35
	Contiguous tissue	0.2398	17.74

selected using a nominal reference density of $\rho = 1000\,kg\,m^{-3}$, corresponding to nominal averaging masses of 1 g and 10 g, respectively. In the adaptive-cube approach, the cube was expanded until the included tissue mass reached the prescribed target mass. In the contiguous-tissue approach, the averaging region was grown from each starting cell by adding face-connected tissue cells across the selected anatomical regions until the target mass was reached.

Table 4 summarizes the maximum SAR values obtained with each method and the corresponding distance from the pointwise SAR maximum, denoted by $d_{SAR_{pw,max}}$. The fixed-volume-cube approach produced the highest averaged SAR values, especially for the 1 g case, and its maximum remained close to the pointwise hotspot. In contrast, the adaptive-cube and contiguous-tissue approaches produced lower peak values and shifted the maximum by approximately 17 mm to 19 mm. This difference arises because the fixed-volume approach averages over the tissue mass contained within a prescribed geometric cube, whereas the adaptive and contiguous approaches enforce the prescribed target mass more directly.

Fig. 5f compares the SAR profiles evaluated from the location of $SAR_{pw,max}$ for the pointwise, fixed-volume-cube, adaptive-cube, and contiguous-tissue approaches. All spatial averaging approaches reduce and broaden the sharp pointwise peak, with a greater reduction for 10 g than for 1 g averaging. These profiles are consistent with the reductions in maximum SAR and the spatial displacements reported in Table 4.

Among the evaluated approaches, the contiguous-tissue method is particularly relevant for the ear geometry, where curved surfaces, cavities, and thin anatomical features make purely geometric cube-based averaging sensitive to the local tissue distribution. By restricting the averaging region to face-connected tissue cells, this approach provides a more anatomically consistent estimate of mass-averaged SAR in the near-ear configuration. For this reason, the contiguous-tissue approach was selected for the 1 g and 10 g averaged SAR distributions shown in Fig. 5d and e.

Overall, the averaging strategy affects both the reported peak SAR value and the location of the maximum, but it does not alter the thermal coupling procedure, for which the local pointwise SAR field is used as the volumetric electromagnetic heat source.

3.3. Temperature response and heating contributions

Fig. 6a shows the absolute temperature distribution obtained from the fully coupled thermal model. The temperature field is dominated by the physiological background distribution, with only a localized elevation near the earbud–tissue interface.

The temperature-increase profiles in Fig. 6b are evaluated from the location of $SAR_{pw,max}$. The total device-induced temperature increase closely follows the electronics-induced contribution, whereas the EM-induced contribution remains substantially smaller over the entire evaluated distance. In contrast to the sharply localized SAR distribution, the temperature response varies smoothly and extends over a broader spatial region because of thermal diffusion.

Fig. 6c and d show the total device-induced temperature increase, ΔT_{all}, obtained by subtracting the bioheat-only solution from the fully coupled solution. This quantity therefore includes heating from both the earbud electronics and electromagnetic absorption. The temperature increase is strongly localized near the earbud and adjacent tissue, remains below 1 °C, and decreases rapidly away from the device.

Fig. 6e and f show the EM-induced temperature increase, ΔT_{EM}, obtained by subtracting the bioheat-plus-electronics solution from the fully coupled solution. The EM-induced response remains localized within the same general near-ear region but is considerably smaller than the total device-induced increase, confirming that device self-heating is the dominant contribution.

The maximum total device-induced temperature increase was 0.905 °C. At the same spatial location, electronics heating contributed 0.882 °C, corresponding to 97.5% of the total increase, whereas electromagnetic absorption contributed 0.0225 °C, corresponding to 2.5%. The separate maximum EM-induced temperature increase was 0.0613 °C and occurred at a different location. These results quantitatively confirm that the predicted temperature response is dominated by heat generated within the earbud electronics rather than by electromagnetic absorption.

Table 5
Sensitivity of the baseline hotspot temperature to blood perfusion and tissue thermal conductivity.

Parameter	Variation	Hotspot temperature (°C)	Change (°C)
–	Baseline	32.47	0.000
Blood perfusion	−20%	32.304	−0.166
	+20%	32.598	+0.128
Thermal conductivity	−10%	32.301	−0.169
	+10%	32.626	+0.156

3.4. Sensitivity to physiological parameters

The baseline maximum total device-induced temperature increase was 0.9046 °C. At this hotspot location, the absolute temperature in the fully coupled baseline simulation was 32.47 °C. Table 5 summarizes the temperature at the same spatial location for the four one-at-a-time sensitivity cases.

Across the investigated parameter variations, the temperature at the baseline near-ear hotspot changed by between −0.169 °C and 0.156 °C relative to the baseline case. Variations in blood perfusion of ±20% produced changes of −0.166 °C and 0.128 °C, while variations in tissue thermal conductivity of ±10% produced changes of −0.169 °C and 0.156 °C. Thus, none of the investigated physiological-property variations changed the predicted temperature at the principal near-ear hotspot by more than approximately 0.17 °C.

3.5. Limitations and practical applications

The present results should be interpreted as a baseline, device-specific assessment rather than as a universal prediction for all commercial earbuds or users. The electromagnetic ear model retains the realistic external ear geometry but represents the tissue as a homogeneous dielectric with skin-equivalent properties. Consequently, local electric-field and SAR magnitudes may differ from those obtained using a fully heterogeneous multilayer anatomical model. Outside the detailed near-ear electromagnetic domain, a uniform background electric field was used to represent low-level exposure within the remaining head tissues. This approximation does not reproduce the detailed attenuation and redistribution of fields across deep anatomical interfaces, and deep-tissue SAR and temperature predictions should therefore be interpreted qualitatively.

The electromagnetic analysis was performed at the shifted resonance of the uncompensated tissue-loaded antenna. Retuning the antenna to 2.45 GHz would require modification of the adopted antenna

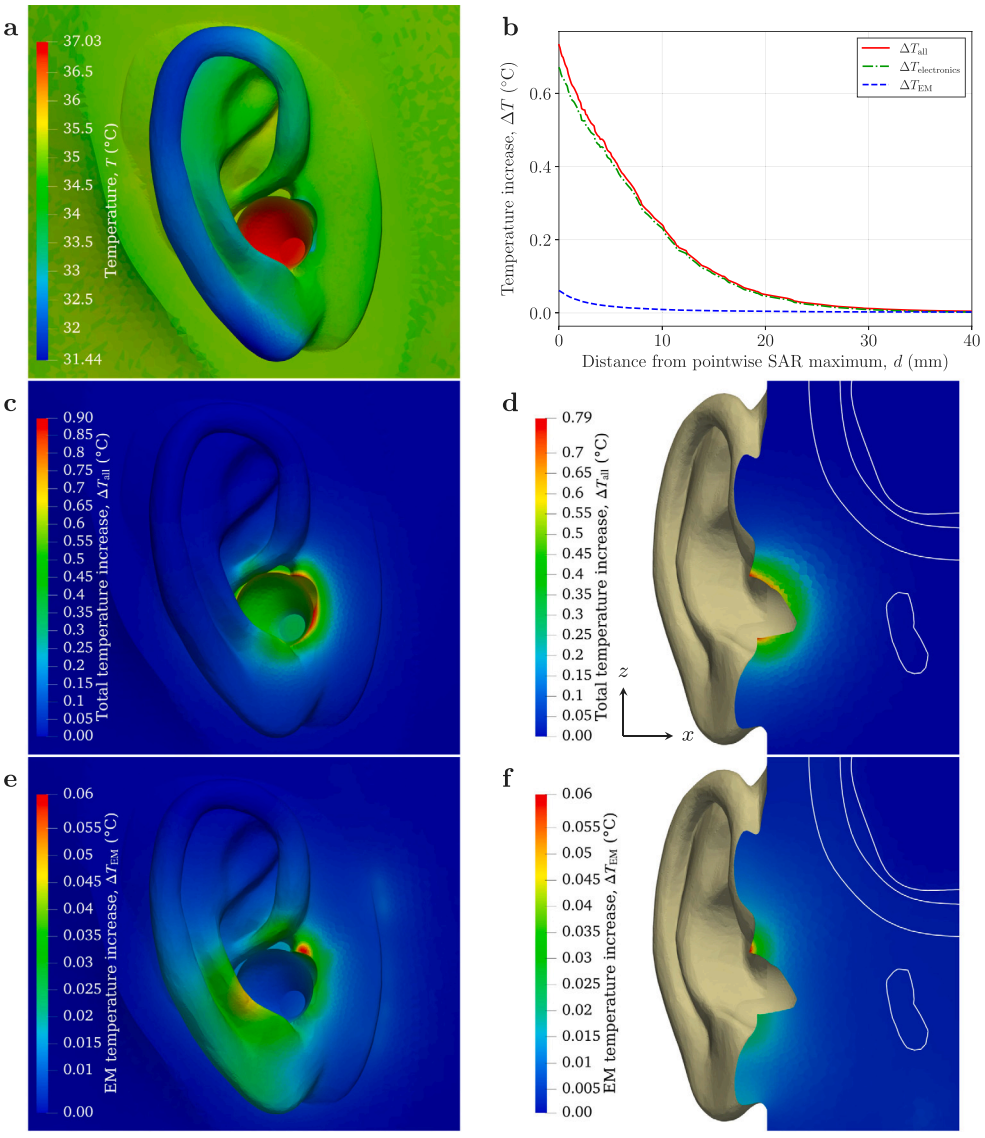


Fig. 6. Spatial temperature response around the ear and the relative contributions of device self-heating and electromagnetic absorption. a, Absolute temperature distribution obtained from the fully coupled thermal model. b, Temperature-increase profiles evaluated from the location of the pointwise SAR maximum, comparing the total device-induced, electronics-induced, and EM-induced contributions. c, Total device-induced temperature increase, ΔT_{all}, including electronics heating and electromagnetic absorption. d, Corresponding ΔT_{all} distribution in the x–z cross-section through the pointwise SAR maximum. e, EM-induced temperature increase, ΔT_{EM}. f, Corresponding ΔT_{EM} distribution in the same x–z cross-section; the white contours in panels d and f delineate material boundaries.

geometry or an additional matching network and would therefore constitute a different antenna design. Accordingly, the reported SAR values characterize the tissue-loaded strong-coupling condition of the investigated antenna rather than the exact operating state of a commercial Bluetooth device matched at 2.45 GHz.

The experimentally identified electronics source is an effective device-level parameter. The simplified electronics domain does not explicitly resolve the battery, integrated circuits, loudspeaker, air cavities, adhesive layers or internal thermal contact resistances. Likewise, the ballistic-gelatin phantom reproduces selected bulk thermal characteristics but does not represent the layered structure of skin and cartilage, blood perfusion, active thermoregulation or inter-individual anatomical variability. The anatomical simulations were restricted to one head geometry, one earbud placement and constant tissue properties. Variations in ear-canal dimensions, contact area, insertion depth and air gaps may affect both conductive heat transfer and electromagnetic coupling. Finally, the head calculations represent the steady-state response under continuous source conditions and do not resolve the time-dependent duty cycle of realistic Bluetooth transmission or intermittent playback.

Despite these limitations, the framework is useful for comparative design-stage analysis. It can be used to investigate how antenna placement and matching, transmitted power, electronics dissipation, enclosure materials, contact area and internal thermal pathways affect local tissue heating. Separating the electronics and electromagnetic contributions allows designers to identify whether thermal mitigation should primarily target RF exposure or device self-heating. The spatially averaged SAR and temperature calculations may also support preliminary or pre-compliance screening against international exposure criteria. These calculations do not replace standardized product-specific compliance measurements.

4. Conclusions

This study developed an integrated experimental–computational framework for predicting the localized thermal response of the human head to an in-ear wireless device. Infrared thermography measurements and a reduced transient earbud–phantom thermal model were used to

identify the effective electronics heat source. Separately, a full-wave near-ear electromagnetic model was used to calculate the spatially resolved SAR distribution, which was subsequently introduced as an electromagnetic heat source in an anatomically resolved Pennes bio-heat model implemented in OpenFOAM. The calibrated thermal model reproduced the mean experimental temperature response with an RMSE of 0.188 °C.

The electromagnetic field and pointwise SAR were strongly localized near the ear, whereas thermal diffusion produced a smoother and more spatially extended temperature response. Under the investigated steady-state continuous-source condition, the maximum total device-induced temperature increase was 0.905 °C. At the same spatial location, electronics heating contributed 0.882 °C, corresponding to 97.5% of the total increase, while electromagnetic absorption contributed 0.0225 °C, corresponding to 2.5%. The separate maximum EM-induced temperature increase was 0.0613 °C and occurred at a different location. These results demonstrate that device self-heating was the dominant heating mechanism for the investigated device configuration and source conditions.

The one-at-a-time sensitivity analysis showed that ±20% variations in blood perfusion and ±10% variations in tissue thermal conductivity changed the temperature at the baseline near-ear hotspot by no more than 0.169 °C. This indicates limited sensitivity of the predicted local temperature to the investigated physiological-property variations.

The proposed framework provides a practical route for combining experimental device characterization, electromagnetic dosimetry, and biological heat-transfer modeling. By separating electronics-induced and electromagnetic heating, the methodology supports comparative design-stage analysis and preliminary thermal assessment of wearable wireless devices. The calculated quantities may assist preliminary or pre-compliance evaluation, but they do not replace standardized product-specific compliance measurements.

CRediT authorship contribution statement

Ivan Dominik Horvat: Writing – review & editing, Writing – original draft, Visualization, Validation, Software, Methodology, Investigation, Formal analysis, Data curation, Conceptualization. **Klementina Vidjak:** Writing – review & editing, Writing – original draft, Visualization, Validation, Methodology, Investigation, Data curation. **Jana Wedel:** Software, Methodology, Investigation, Data curation, Conceptualization. **Jurij Iljaž:** Methodology, Investigation, Conceptualization. **Blaž Kamenik:** Methodology. **Dragan Poljak:** Writing – review & editing, Writing – original draft, Validation, Supervision, Resources, Project administration, Funding acquisition, Conceptualization. **Jure Ravnik:** Writing – review & editing, Supervision, Project administration, Methodology, Investigation, Formal analysis, Conceptualization.

Ethical approval/institutional review board statement

This study did not involve experiments on human participants, animals, or the collection of identifiable human data. The experimental component was performed using a tissue-mimicking ballistic-gelatin ear phantom, and the remaining analyses were computational simulations based on published anatomical and tissue-property data. Therefore, ethical committee or Institutional Review Board approval was not required.

Declaration of generative AI and AI-assisted technologies in the manuscript preparation process

During the preparation of this work, the authors used ChatGPT by OpenAI for language editing, grammar improvement, and assistance in assembling grammatically corrected sentences. The authors reviewed and edited the output as needed and take full responsibility for the content of the published article.

Funding statement

This work was supported by the Slovenian Research and Innovation Agency, project J7-60118, and the Croatian Science Foundation, project IPS-2024-02-7779.

Declaration of competing interest

The authors declare that they have no known competing financial interests or personal relationships that could have appeared to influence the work reported in this paper.

Acknowledgments

The authors gratefully acknowledge Prof. Cavagnaro for valuable discussions and for assistance with the simulations. The authors thank the Slovenian Research and Innovation Agency, project J7-60118, and the Croatian Science Foundation, project IPS-2024-02-7779.

Appendix A. Supplementary data

Supplementary material related to this article can be found online at https://doi.org/10.1016/j.jtherbio.2026.104570.

Data availability

The data supporting the findings of this study are not publicly available at the time of submission because the complete datasets include large electromagnetic and thermal simulation output files, geometry-dependent processed fields, and solver-specific configuration files that require contextual information for correct interpretation. The processed data underlying the main figures and tables are available from the corresponding author upon reasonable request.

References

Ailawalia, P., Marin, M., Kaur, J., 2025. A study of thermoelastic double porosity rod under a thermal shock. J. Appl. Comput. Mech. 11 (3), 707–714. http://dx.doi.org/10.22055/jacm.2024.47432.4710.

Alali, Z., Eckels, S., 2024. 3D numerical simulations of mixed convective heat transfer and correlation development for a thermal manikin head. Heliyon 10 (9), e30161. http://dx.doi.org/10.1016/j.heliyon.2024.e30161.

Bauer, J., Górecki, I., Kohyt, M., Migasiewicz, A., Podbielska, H., 2018. The influence of smartphones' operation modes on the superficial temperature distribution in the human auricle region. J. Therm. Anal. Calorim. 133 (1), 559–569. http://dx.doi.org/10.1007/s10973-018-7047-8.

Bauer, J., O'Mahony, C., Chovan, D., Mulcahy, J., Silien, C., Tofail, S.A., 2019. Thermal effects of mobile phones on human auricle region. J. Therm. Biol. 79, 56–68. http://dx.doi.org/10.1016/j.jtherbio.2018.11.008, URL https://www.sciencedirect.com/science/article/pii/S0306456518304431.

Bluetooth Special Interest Group, 2021. Bluetooth Core Specification Version 5.3. vol. 2, Part A, Bluetooth SIG, p. 390.

Cardis, E., Deltour, I., Mann, S., Moissonnier, M., Taki, M., Varsier, N., Wake, K., Wiart, J., 2008. Distribution of RF energy emitted by mobile phones in anatomical structures of the brain. Phys. Med. Biol. 53 (11), 2771. http://dx.doi.org/10.1088/0031-9155/53/11/001.

Christopher, B., Mary Y, S., Khandaker, M.U., Jojo, P., 2021. Empirical study on specific absorption rate of head tissues due to induced heating of 4G cell phone radiation. Radiat. Phys. Chem. 178, 108910. http://dx.doi.org/10.1016/j.radphyschem.2020.108910, the 2nd International Forum on Advances in Radiation Physics (IFARP-2). URL https://www.sciencedirect.com/science/article/pii/S0969806X20302085.

Dassault Systèmes, 2025. Vélizy-Villacoublay, France, CST studio suite. URL https://www.3ds.com/products/simulia/cst-studio-suite.

De Dear, R.J., Arens, E., Hui, Z., Oguro, M., 1997. Convective and radiative heat transfer coefficients for individual human body segments. Int. J. Biometeorol. 40 (3), 141–156. http://dx.doi.org/10.1007/s004840050035.

Diao, Y., Joseph, W., Poljak, D., Giaccone, L., Kodera, S., Laakso, I., Yamazaki, K., Li, K., Sasaki, K., Tanghe, E., Cvetković, M., El Hajj, W., Hikage, T., Kaburcuk, F., Schmid, G., Nejašmić, A. Šušnjara, Tarnaud, T., Anderson, V., Foster, K.R., Samaras, T., Tell, R.A., Watanabe, S., Chou, C.-K., Hirata, A., 2025. Recent advances and future perspective in computational bioelectromagnetics for exposure assessments. Bioelectromagnetics 46 (3), e70002. http://dx.doi.org/10.1002/bem.70002, URL https://onlinelibrary.wiley.com/doi/abs/10.1002/bem.70002.

Drizdal, T., van Rhoon, G.C., Fiser, O., Vrba, D., van Holthe, N., Vrba, J., Paulides, M.M., 2023. Assessment of the thermal tissue models for the head and neck hyperthermia treatment planning. J. Therm. Biol. 115, 103625. http://dx.doi.org/10.1016/j.jtherbio.2023.103625, URL https://www.sciencedirect.com/science/article/pii/S0306456523001663.

Etehadtavakol, M., Ng, E., 2020. Survey of numerical bioheat transfer modelling for accurate skin surface measurements. Therm. Sci. Eng. Prog. 20, 100681. http://dx.doi.org/10.1016/j.tsep.2020.100681, URL https://www.sciencedirect.com/science/article/pii/S2451904920302018.

FLIR, 2025. FLIR A655sc high-resolution science grade LWIR camera. Product webpage. URL https://www.flir.com/products/a655sc/. (Accessed 27 October 2025).

Health Protection Agency (HPA), 2012. Health Effects from Radiofrequency Electromagnetic Fields: The Report of the Independent Advisory Group on Non-Ionising Radiation (AGNIR). Tech. Rep. 20, Health Protection Agency.

Hirata, A., Kodera, S., Sasaki, K., Gomez-Tames, J., Laakso, I., Wood, A., Watanabe, S., Foster, K.R., 2021. Human exposure to radiofrequency energy above 6 GHz: review of computational dosimetry studies. Phys. Med. Biol. 66 (8), http://dx.doi.org/10.1088/1361-6560/abf1b7.

Hirata, A., Laakso, I., Apollonio, F., Kodera, S., Kubota, Y., Lan, J., Li, K., Liberti, M., Poljak, D., Sasaki, K., Zhadobov, M., Diao, Y., 2025. Model variability in assessment of human exposure to radiofrequency fields. http://dx.doi.org/10.36227/techrxiv.176118014.43813083/v1, TechRxiv 2025 (1023). URL https://www.techrxiv.org/doi/abs/10.36227/techrxiv.176118014.43813083/v1.

Horvat, I., Iljaž, J., 2025. Numerical modeling of non-Fourier bioheat transfer in multilayer biological tissue using BEM to simulate dynamic thermography in skin tumor diagnostics. EABE 179, 106408. http://dx.doi.org/10.1016/j.enganabound.2025.106408.

Hristov, J., 2019. Bio-heat models revisited: Concepts, derivations, nondimensalization and fractionalization approaches. Front. Phys. 7 - 2019, http://dx.doi.org/10.3389/fphy.2019.00189, URL https://www.frontiersin.org/journals/physics/articles/10.3389/fphy.2019.00189.

Hymczak, H., Gołąb, A., Mendrala, K., Plicner, D., Darocha, T., Podsiadło, P., Hudziak, D., Gocol, R., Kosiński, S., 2021. Core temperature measurement-principles of correct measurement, problems, and complications. Int. J. Environ. Res. Public Health 18 (20), 10606. http://dx.doi.org/10.3390/ijerph182010606.

IEEE, 2019. IEEE Standard for Safety Levels with Respect to Human Exposure to Electric, Magnetic, and Electromagnetic Fields, 0 Hz to 300 GHz. IEEE Std C95.1-2019 (Revision of IEEE Std C95.1-2005/Incorporates IEEE Std C95.1-2019/Cor 1-2019), http://dx.doi.org/10.1109/IEEESTD.2019.8859679.

International Commission on Non-Ionizing Radiation Protection (ICNIRP), 2020. Guidelines for limiting exposure to electromagnetic fields (100 khz to 300 GHz). Health Phys. 118 (5), 483–524.

IT'IS Foundation, 2024. Tissue Properties Database V4.2. http://dx.doi.org/10.13099/VIP21000-04-2.

Karipidis, K., Mate, R., Urban, D., Tinker, R., Wood, A., 2021. 5G mobile networks and health—a state-of-the-science review of the research into low-level RF fields above 6 GHz. J. Expo. Sci. Environ. Epidemiology 31 (4), 585–605. http://dx.doi.org/10.1038/s41370-021-00297-6.

Khan, M.A., Bibi, M., Jahangir, A., Rahman, A., Riaz, U., Rahman, S., Iqbal, S., Zaheer, S., 2026. Multiphysics modeling and sensitivity analysis of temperature-dependent rayleigh waves in rotating magneto-thermoelastic semiconductor systems with hall current effects. J. Complex Multiphysics Eng. Syst. 1, 219–238. http://dx.doi.org/10.56578/jcmes010301.

Kim, S., Sharif, Y.A., Nasim, I., 2024. Human electromagnetic field exposure in wearable communications systems: A review. e-Prime - Adv. Electr. Eng. Electron. Energy 8, 100508. http://dx.doi.org/10.1016/j.prime.2024.100508, URL https://www.sciencedirect.com/science/article/pii/S2772671124000901.

Li, K., Diao, Y., Sasaki, K., Prokop, A., Poljak, D., Doric, V., Xi, J., Kodera, S., Hirata, A., Hajj, W.E., 2021. Intercomparison of calculated incident power density and temperature rise for exposure from different antennas at 10–90 GHz. IEEE Access 9, 151654–151666. http://dx.doi.org/10.1109/ACCESS.2021.3126738.

Li, K., Kodera, S., Poljak, D., Diao, Y., Sasaki, K., Šušnjara, A., Prokop, A., Taguchi, K., Xi, J., Zhang, S., Yao, M., Sacco, G., Zhadobov, M., Hajj, W.E., Hirata, A., 2023. Calculated epithelial/absorbed power density for exposure from antennas at 10–90 GHz: Intercomparison study using a planar skin model. IEEE Access 11, 7420–7435. http://dx.doi.org/10.1109/ACCESS.2023.3238582.

Li, K., Kodera, S., Poljak, D., Diao, Y., Sasaki, K., Zhang, S., Yao, M., Kapetanovic, A., Li, C., Wu, T., Liebig, T., Simon, W., Hirata, A., 2024. Spatially averaged epithelial/absorbed power density for nonplanar skin models exposed to antenna at 10–90 GHz. IEEE Access 12, 15379–15389. http://dx.doi.org/10.1109/ACCESS.2024.3358109.

Li, K., Kodera, S., Poljak, D., Prokop, A., Diao, Y., Zhang, S., Yao, M., Li, C., Wu, T., Liebig, T., Simon, W., Škiljo, M., Hirata, A., 2026. Intercomparisons of computed epithelial/absorbed power density and temperature rise in anatomical human face models under localized exposures at 10 GHz and 30 GHz. Phys. Med. Biol. 71 (1), 01NT02. http://dx.doi.org/10.1088/1361-6560/ae2ce1.

Megahid, S.F., 2025. Two-dimensional biothermomechanical effects in a layer of skin tissue exposed to variable thermal loading using a fourth-order MGT model. Sci. Rep. 15 (1), 17023. http://dx.doi.org/10.1038/s41598-025-01745-1.

Megahid, S.F., 2026a. Electromagnetothermoelastic analysis of skin tissue using a Mittag–Leffler memory kernel in the dual-phase lag framework. Arch. Appl. Mech. 96 (7), 134. http://dx.doi.org/10.1007/s00419-026-03133-1.

Megahid, S.F., 2026b. Magneto-poroelastic responses in triple-phase lag thermoelastic media. Arch. Appl. Mech. 96 (5), 101. http://dx.doi.org/10.1007/s00419-026-03086-5.

Megahid, S.F., 2026c. Thermoelastic response in skin tissue exposed to laser radiation via the Moore–Gibson–Thompson model containing higher-order memory-dependent derivatives. Acta Mech. 237 (3), 1317–1339. http://dx.doi.org/10.1007/s00707-025-04519-y.

Noetscher, G.M., Yanamadala, J., Makarov, S.N., Pascual-Leone, A., 2014. Comparison of cephalic and extracephalic montages for transcranial direct current stimulation—A numerical study. IEEE Trans. Biomed. Eng. 61 (9), 2488–2498. http://dx.doi.org/10.1109/TBME.2014.2322774.

OpenFOAM Foundation, 2023. Openfoam v11. URL https://www.openfoam.org.

Padgette, J., Bahr, J., Batra, M., Smithbey, R., Chen, L., Scarfone, K., 2022. Guide to bluetooth security. http://dx.doi.org/10.6028/NIST.SP.800-121r2-upd1, URL https://tsapps.nist.gov/publication/get_pdf.cfm?pub_id=934038.

Pennes, H.H., 1948. Analysis of tissue and arterial blood temperatures in the resting human forearm. J. Appl. Physiol. 1 (2), 93–122. http://dx.doi.org/10.1152/jappl.1948.1.2.93.

Razek, A., 2023. Assessment and categorization of biological effects and atypical symptoms owing to exposure to RF fields from wireless energy devices. Appl. Sci. 13 (3), http://dx.doi.org/10.3390/app13031265.

Salem, M., Abouelregal, A., Elzayady, M., Sedighi, H.M., 2024. Biomechanical response of skin tissue under ramp-type heating by incorporating a modified bioheat transfer model and the atangana–baleanu fractional operator. Acta Mech. 235, 1–20. http://dx.doi.org/10.1007/s00707-024-03988-x.

Scientific Committee on Emerging and Newly Identified Health Risks (SCENIHR), 2015. Potential Health Effects of Exposure to Electromagnetic Fields (EMF). Tech. rep., European Commission.

Thermtest Inc., 2024. ABS - acrylonitrile butadiene styrene | thermal conductivity, specific heat, density. URL https://thermtest.com/thermal-resources/materials-database. (Accessed 23 September 2025).

Verma, A., Kumar, V., Gupta, S., 2023. Bio-effects of 5th generation electromagnetic waves on organs of human beings. Glob. Health J. 7 (4), 206–211. http://dx.doi.org/10.1016/j.glohj.2023.11.005, URL https://www.sciencedirect.com/science/article/pii/S241464472300091X.

Vidjak, K., Škiljo, M., Poljak, D., 2025. Computational study of 5G technology dosimetry on SAM human head model. In: 2025 International Conference on Software, Telecommunications and Computer Networks. SoftCOM, pp. 1–6. http://dx.doi.org/10.23919/SoftCOM66362.2025.11197332.

Virtanen, P., Gommers, R., Oliphant, T.E., Haberland, M., Reddy, T., Cournapeau, D., Burovski, E., Peterson, P., Weckesser, W., Bright, J., van der Walt, S.J., Brett, M., Wilson, J., Millman, K.J., Mayorov, N., Nelson, A.R.J., Jones, E., Kern, R., Larson, E., Carey, C.J., Polat, İ., Feng, Y., Moore, E.W., VanderPlas, J., Laxalde, D., Perktold, J., Cimrman, R., Henriksen, I., Quintero, E.A., Harris, C.R., Archibald, A.M., Ribeiro, A.H., Pedregosa, F., van Mulbregt, P., SciPy 1.0 Contributors, 2020. SciPy 1.0: Fundamental algorithms for scientific computing in python. Nature Methods 17, 261–272. http://dx.doi.org/10.1038/s41592-019-0686-2.

Wake, K., Varsier, N., Watanabe, S., Taki, M., Wiart, J., Mann, S., Deltour, I., Cardis, E., 2009. The estimation of 3D SAR distributions in the human head from mobile phone compliance testing data for epidemiological studies. Phys. Med. Biol. 54 (19), 5695. http://dx.doi.org/10.1088/0031-9155/54/19/003.

Winter, J., Shifler, C., 1975. The Material Properties of Gelatin Gels. BRL Contract Report No. 217 AD-A008396, U.S. Army Ballistic Research Laboratories, URL https://apps.dtic.mil/sti/tr/pdf/ADA008396.pdf.

Woo, T.H., Joong Yoon, Y., 2021. Bent loop inverted F antenna for TWS bluetooth earphones. In: 2020 International Symposium on Antennas and Propagation. ISAP, pp. 319–320. http://dx.doi.org/10.23919/ISAP47053.2021.9391238.

Xu, X., Rioux, T.P., Castellani, M.P., 2023. Three dimensional models of human thermoregulation: A review. J. Therm. Biol. 112, 103491. http://dx.doi.org/10.1016/j.jtherbio.2023.103491, URL https://www.sciencedirect.com/science/article/pii/S0306456523000323.

Yun, J., Yoo, Y.J., Kim, H.R., Song, Y.M., 2023. Recent progress in thermal management for flexible/wearable devices. Soft Sci. 3 (2), http://dx.doi.org/10.20517/ss.2023.04, URL https://www.oaepublish.com/articles/ss.2023.04.